Supplementary Information for

Microbial community dynamics and stability during an ammonia-induced shift to syntrophic acetate oxidation

Jeffrey J. Werner[1,2], Marcelo L. Garcia[3], Sarah D. Perkins[3], Kevin E. Yarasheski[4], Samuel R. Smith[†,4], Brian D. Muegge[5], Frank J. Stadermann[†,6], Christopher M. DeRito[7], Christine Floss[6], Eugene L. Madsen[7], Jeffrey I. Gordon[5], Largus T. Angenent[1,*]

1. Department of Biological and Environmental Engineering, Cornell University, Ithaca, NY 14853
2. Chemistry Department, SUNY Cortland, Cortland, NY 13045
3. Department of Energy, Environmental and Chemical Engineering, Washington University, St. Louis, MO 63130
4. Department of Internal Medicine, Washington University School of Medicine, St. Louis, MO 63108
5. Center for Genome Sciences and Systems Biology, Washington University School of Medicine, St. Louis, MO 63108
6. Department of Physics, Washington University, St. Louis, MO 63130
7. Department of Microbiology, Cornell University, Ithaca, NY 14853

* Please address correspondence to L.T.A. (e-mail: la249@cornell.edu)
† Author is deceased

Contents

Methods: DNA-SIP

The serum-bottle-based anaerobic acetate oxidation assays were dosed with both [13]C- and unlabeled acetate. Biomass samples from duplicate serum bottles were gathered on 0.22 μm filters; these were pooled, DNA was extracted, and, then processed by ultracentrifugation (separation of [13]C- from ^{12}C-DNA), and clean up, as previously described (1-3). The heavy (^{13}C-labeled) DNA was operationally defined as the lowest dilution of cesium-chloride-separated DNA that yielded a PCR amplicon of 16S rRNA gene in the ^{13}C treatment while failing to yield and amplicon in the ^{12}C treatment.

References:

1. **DeRito CM, Pumphrey GM, Madsen EL.** 2005. Use of field-based stable isotope probing to identify adapted populations and track carbon flow through a phenol-degrading soil microbial community. Appl Environ Microbiol **71**:7858-7865.
2. **Liou JS, Derito CM, Madsen EL.** 2008. Field-based and laboratory stable isotope probing surveys of the identities of both aerobic and anaerobic benzene-metabolizing microorganisms in freshwater sediment. Environ Microbiol **10**:1964-1977.
2. **Padmanabhan P, Padmanabhan S, DeRito C, Gray A, Gannon D, Snape JR** *et al*. 2003. Respiration of ^{13}C-labeled substrates added to soil in the field and subsequent 16S rRNA gene analysis of ^{13}C-labeled soil DNA. Appl. Environ. Microbiol. **69**:1614-1622.

Methods: NanoSIMS

The NanoSIMS measurements with hybridized samples were carried out using the Cameca NanoSIMS 50 ion microprobe. A ~1pA 16 keVCs$^+$ primary beam (~100 nm in diameter) was rastered over individual sample areas and secondary ions of $^{13}C^-$, $^{12}C_2^-$, $^{28}Si^-$ and $^{127}I^-$ were collected simultaneously in four separate electron multipliers, along with secondary electrons. The primary beam was rastered over areas of 20 x 20 μm in an automated mapping mode with automatic stage movement that allowed sequential measurement of raster areas following a predefined grid pattern. Each analysis consisted of between 10 and 25 individual layers that are subsequently added together to constitute a single image measurement of 256^2 pixels. Measurement times varied with the number layers acquired but were generally on the order of 2 to 3 h; the acquisition rate was 10 ms per pixel. Images were corrected for sample drift from layer to layer and were checked for statistical outliers.

Supplementary Table S1. Biological samples taken from swine waste digesters for bacterial 16S rRNA gene sequencing and shotgun sequencing, with corresponding reactor conditions that had been changed during the interim period as described in the text of the research paper.

Day	Reactor	T (°C)	Ammonia (g N L^{-1})	SLR (g VS L^{-1} d^{-1})	Syntrophic acetate oxidation (%)	Bacterial 16S rRNA gene sequences (GenBank accession numbers)	Shotgun sequences (MG-RAST sample ID)
360	R1	25	1.2	4.0	na [a]	275 sequences (GQ138118 - GQ138392)	na
	R2	25	1.2	4.0	na	320 sequences (GQ132191 - GQ132510)	na
	R3	25	1.2	4.0	na	313 sequences (GQ133120 - GQ133432)	na
	R4	25	1.2	4.0	na	309 sequences (GQ134125 - GQ134433)	na
700	R1	25	1.6	2.2	na	286 sequences (GQ138393 - GQ138678)	na
	R2	25	1.6	2.2	na	155 sequences (GQ132511 - GQ132665)	na
	R3	25	4.4	2.2	na	183 sequences (GQ133433 - GQ133615)	na
	R4	25	4.4	2.2	na	237 sequences (GQ134434 - GQ134670)	na
809	R1	35	1.8	2.2	5%	230 sequences (GQ138679 - GQ138908)	155,222 reads (Plate1_Region1_TCA R1; 4444124)
	R2	35	1.8	2.2	na	250 sequences (GQ132666 - GQ132915)	162,142 reads (P1R2; 4444183)
	R3	35	4.4	2.2	5%	283 sequences (GQ134671 - GQ134953)	247,178 reads (P1R3; 4444185)
	R4	35	4.4	2.2	2%	215 sequences (GQ133616 - GQ133830)	216,610 reads (P1R4; 4444186)
914	R1	35	1.8	2.2	5%	291 sequences (GQ138909 - GQ139199)	210,933 reads (P2R1; 4444187)
	R2	35	1.8	2.2	na	204 sequences (GQ132916 - GQ133119)	179,608 reads (P2R2; 4444188)
	R3	35	4.9	2.2	25%	294 sequences (GQ133831 - GQ134124)	224,844 reads (P2R3; 4444190)
	R4	35	4.9	2.2	18%	275 sequences (GQ134954 - GQ135228)	212,055 reads (P2R4; 4444194)

(a) "na" = not measured
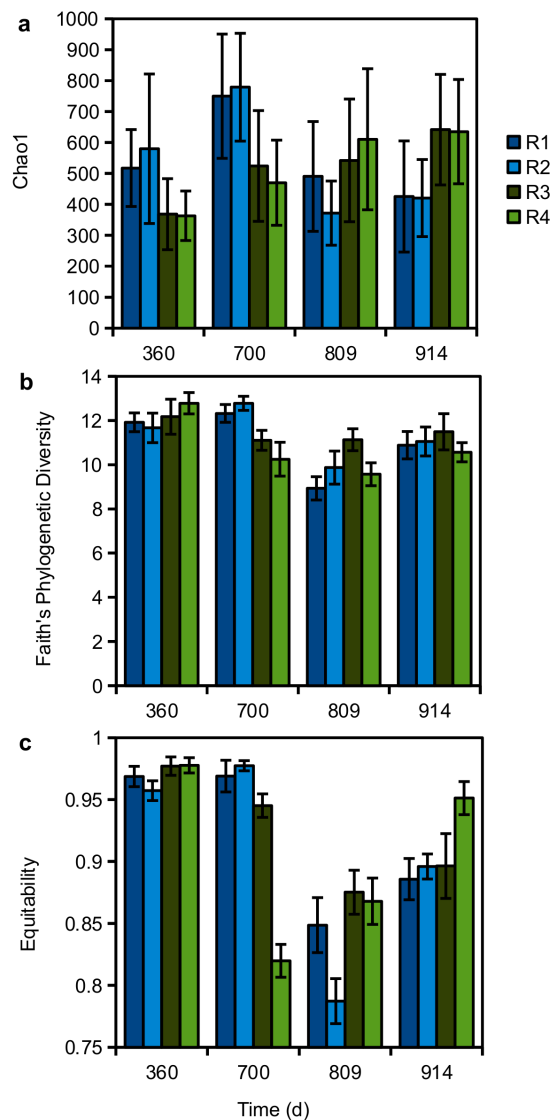
Supplementary Figure S1. Alpha diversity measures of OTU profiles (97% ID) determined using bacterial 16S rRNA gene characterizations from reactor samples R1-R4: (**a**) Chao1 estimate of diversity, (**b**) Faith's PD, and (**c**) equitability (a measure of evenness). Error bars represent the SD of 100 rarefactions of 100 sequences each.
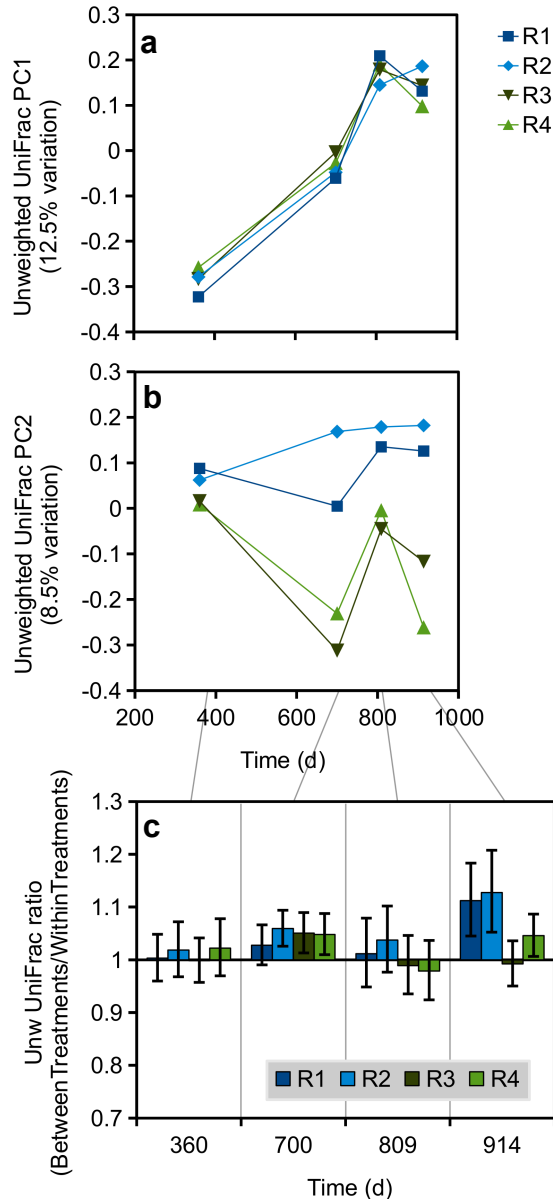
Supplementary Figure S2. Unweighted UniFrac distances between bacterial 16S rRNA gene characterizations for R1-R4: (**a**) UniFrac principal coordinate 1 as a function of time, (**b**) UniFrac principal coordinate 2 as a function of time, and (**c**) for each time point, ratio of between-treatment distances to within-treatment distances. In other words, the distance between experimental reactors and control reactors, divided by the distance between replicate reactors (ratio greater than 1 means that the reactor was closer to the other with the same treatment than to the reactors with the different treatment). In graphs (**a**) and (**b**), sample similarity can be judged by the distance between points along the *y*-axis; each principal coordinate shows a different dimension of variability in the UniFrac data. Error bars in (**c**) represent the SD of ratios from 20 rarefactions of 100 sequences each (SD values were calculated for log-ratios, as errors in ratios of two normal distributions are log-normally distributed; as a result, the (+) error bars are slightly longer than the (-) error bars).
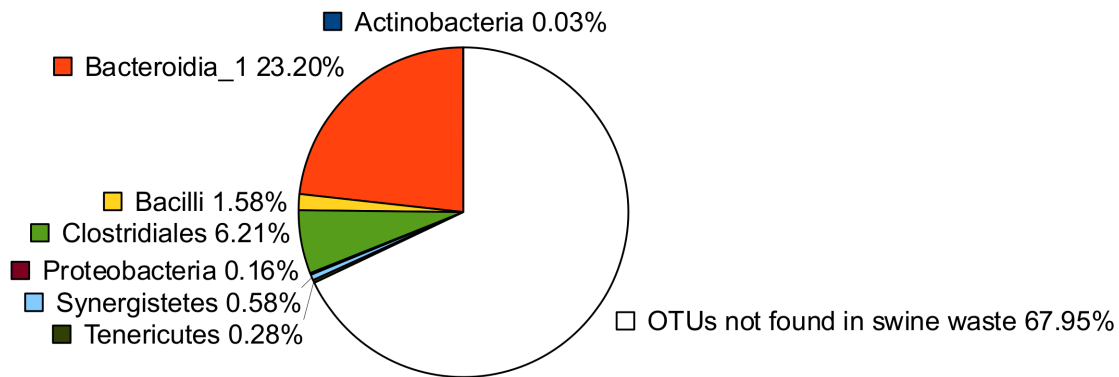
Supplementary Figure S3. Taxonomic distribution of OTUs found both in swine waste and reactor samples. Percentages shown were normalized to relative abundance. The white portion, "OTUs not found in swine waste," represents the proportion of reactor OTUs that we did not detect in the swine waste. The data suggest that most of the OTUs that were high abundance in both swine waste and reactor samples were within the class Bacteroidia 1.
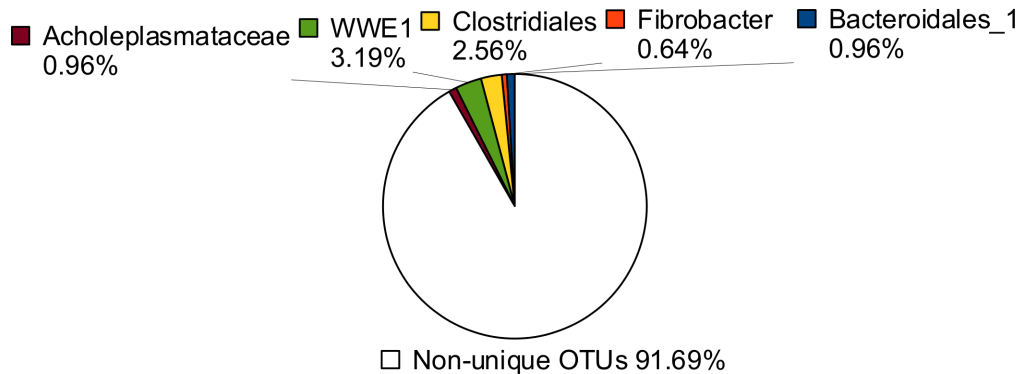
Supplementary Figure S4. Taxonomic distribution of OTUs found only in samples for which syntrophic acetate oxidation was elevated (R3 and R4 at day 914). Percentages shown were normalized to average relative abundance. The white portion, "Non-unique OTUs," represents the proportion of OTUs in R3 and R4 at day 914 that were not unique to that condition (i.e., OTUs that also showed up when syntrophic acetate oxidation was not elevated). OTUs that were unique to high syntrophic acetate oxidation conditions made up a total of only 8.3% of the total community.
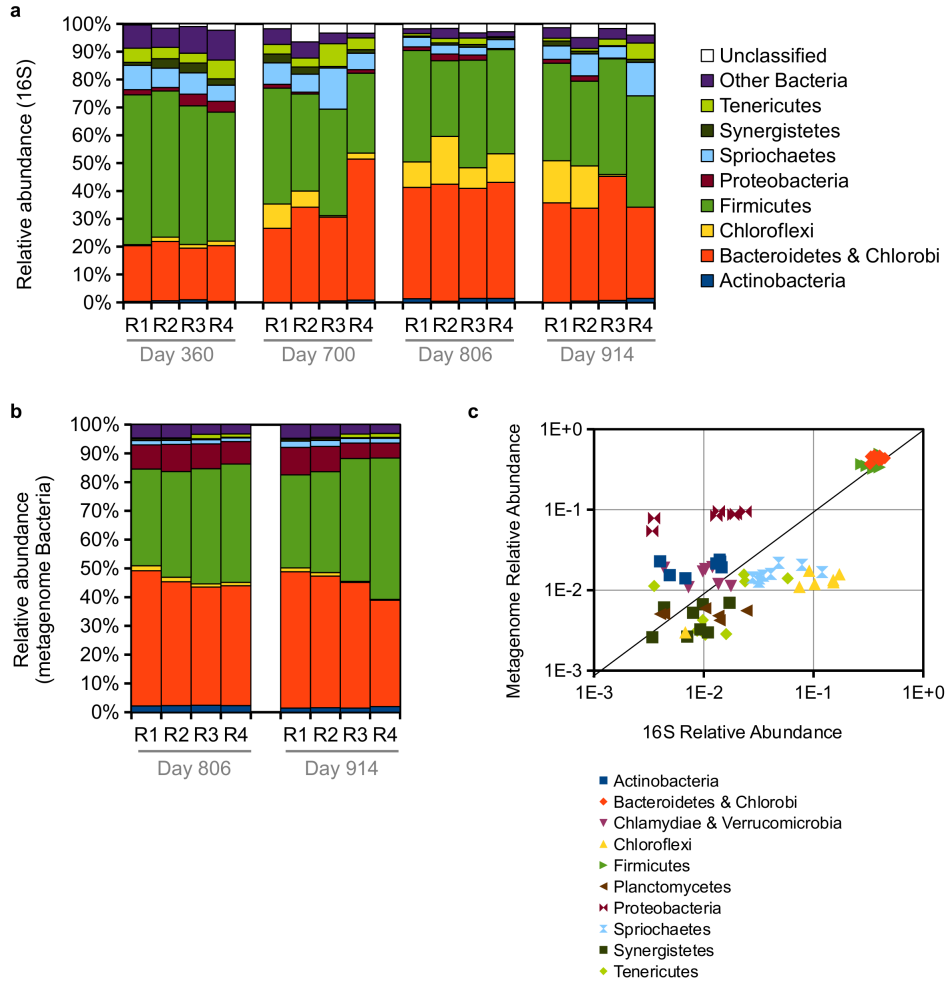
Supplementary Figure S5. Relative abundance of bacterial taxonomic divisions, determined from (**a**) near full-length bacterial 16S rRNA gene characterizations and (**b**) shotgun sequencing of community DNA. Also, to compare results from the same samples, (**c**) shows a plot of relative abundance results from 16S rRNA gene sequencing *vs*. bacterial reads from shotgun pyrosequencing. Note the $\log_{10}$ scale on both axes in (**c**). Consensus taxonomies were assigned to shotgun reads with MEGAN using the results of a BLASTX search of raw shotgun reads *vs*. NCBI-nr. For comparison to bacterial 16S rRNA gene sequences, the shotgun reads were summarized only for those assigned to Bacteria (~5-10% of shotgun reads were Archaeal; see **Fig. 5** in the main text).
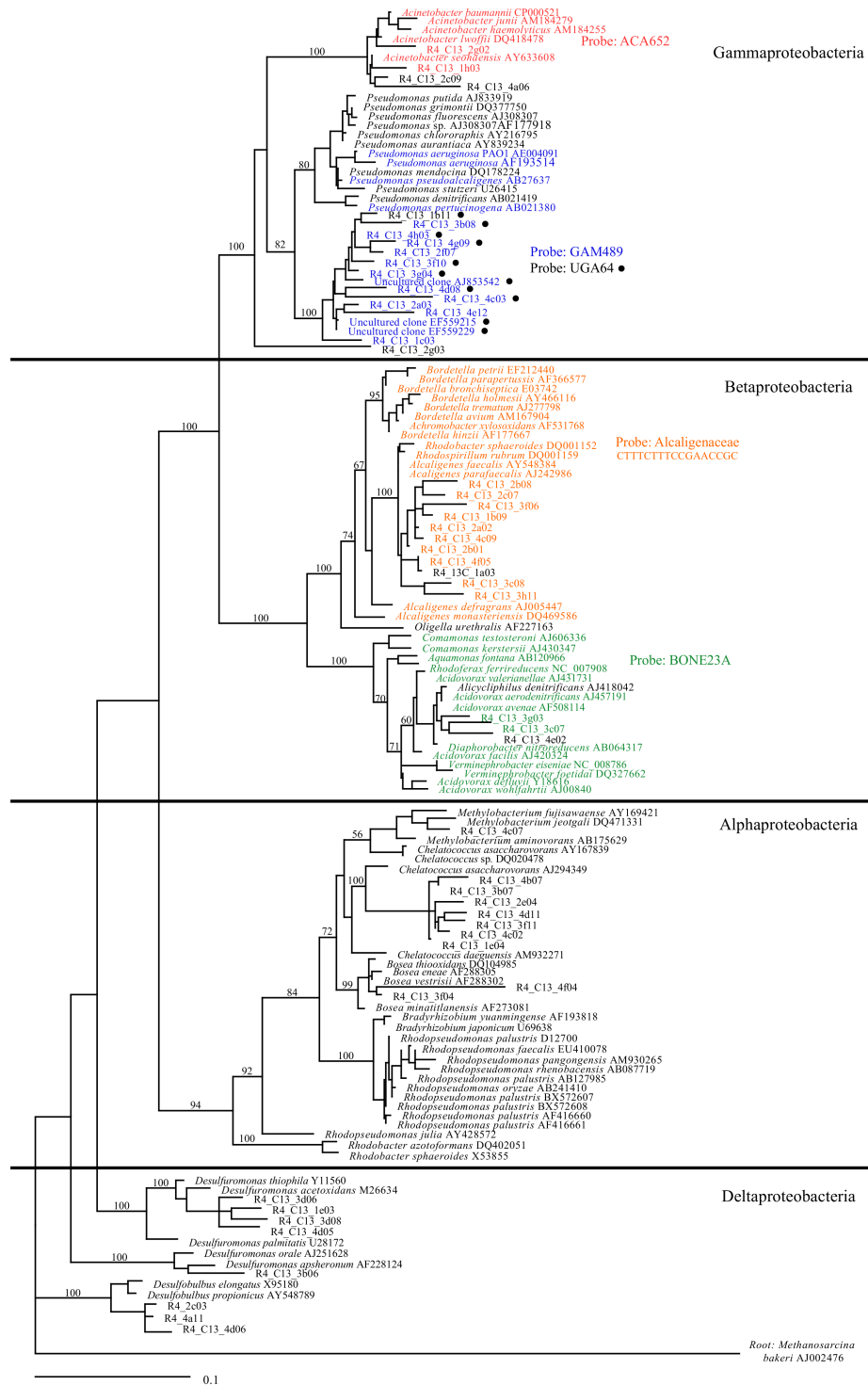
Supplementary Figure S6. Maximum-likelihood phylogenetic tree of Proteobacteria 16S rRNA gene amplicons enriched from ^{13}C-labeled acetate assays by DNA-SIP (R4; day 982). Highlighted phylotypes are predicted to be targeted by the probes indicated to the right. The probe chosen for later FISH-NanoSIMS in this study, GAM489, is highlighted in blue.

A. [^{13}C] Organisms that took up ^{13}C-labeled acetate

B. [^{127}I] Organisms labeled with probe GAM489

C. [^{12}C] Overall carbon-12 signal from FISH-nanoSIMS

D. SE

2 μ
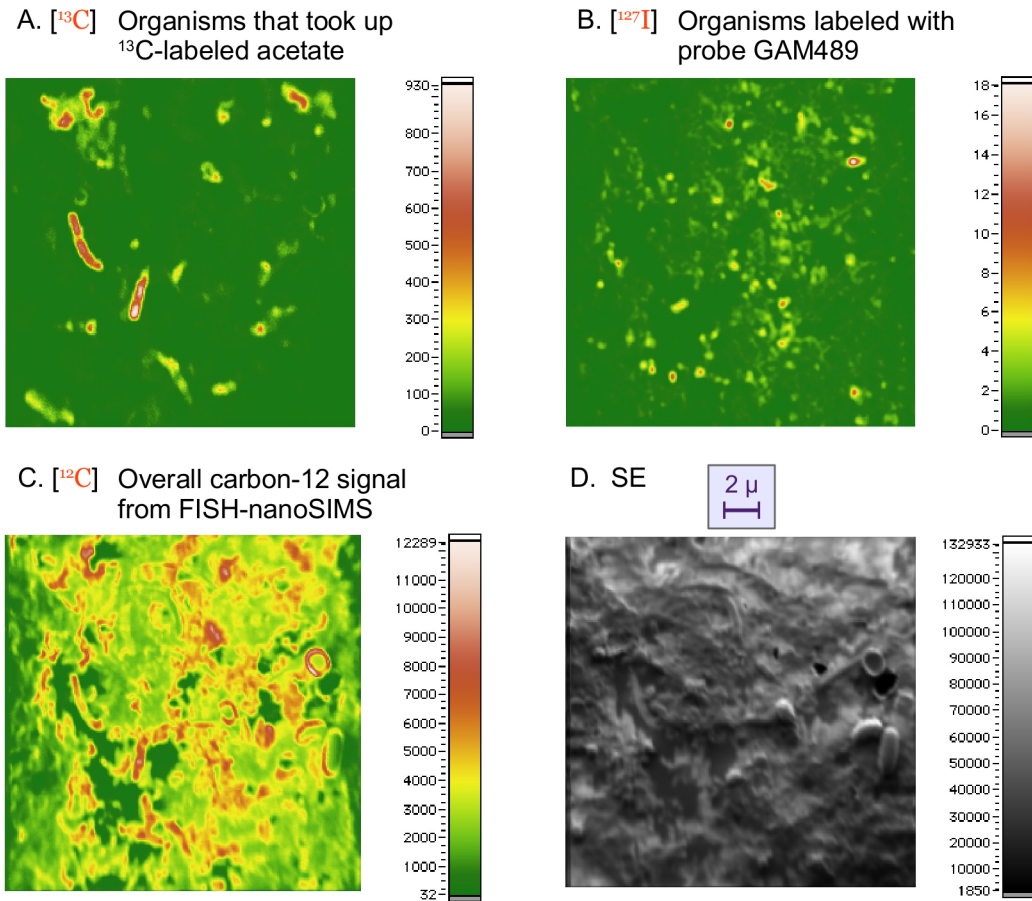
Supplementary Figure S7. An example frame of FISH–NanoSIMS images from an enrichment from R4, day 982 (syntrophic acetate oxidation 18%): (**a**) ^{13}C FISH–NanoSIMS image highlighting incorporation of the methyl carbon from ^{13}C-labeled acetate; (**b**) ^{127}I FISH–NanoSIMS image highlighting localization of the isotopically-labeled GAM489 probe for *Pseudomonas* sp.; (**c**) ^{12}C FISH–NanoSIMS image surveying the overall signal from carbon; and (**d**) SE image from the same frame. Scale bar indicates width of 2 μm (total image is 20 × 20 μm). Note that *Pseudomonas* spp. cells in (**b**) did not correspond with ^{13}C-enriched organisms in (**a**). Similar negative results were obtained from six independent analyses.
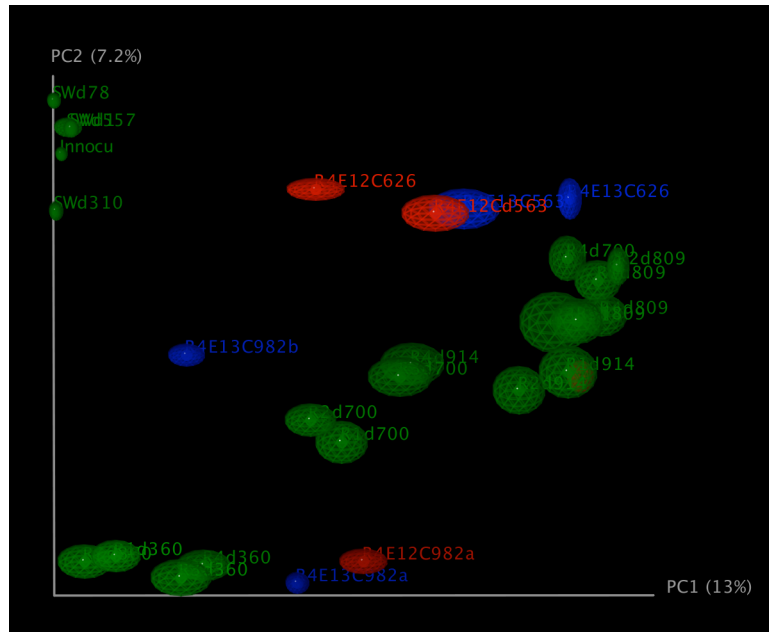
Supplementary Figure S8. Divergence of acetate-enrichment tests from the reactor (R4) community for operating days 563, 626, and 982 indicated that resultant communities in bottle tests were not representative of the conditions in the reactors (R1-R4) for day 360, 700, 809, and 914 and in R4 for day 982: A Principal Coordinates analysis (PCoA) of unweighted UniFrac distances (bacterial 16S rRNA gene characterizations) showed that enrichment experiments (blue and red) resulted in bacterial communities that were very different from the reactor samples (green). In addition, the communities resulting from bottle assays were not reproducible (i.e., replicate assays were not close to each other in UniFrac distance). Clouds surrounding each sample point represent the variation of sample position within 100 rarefactions, 100 seq/sample.
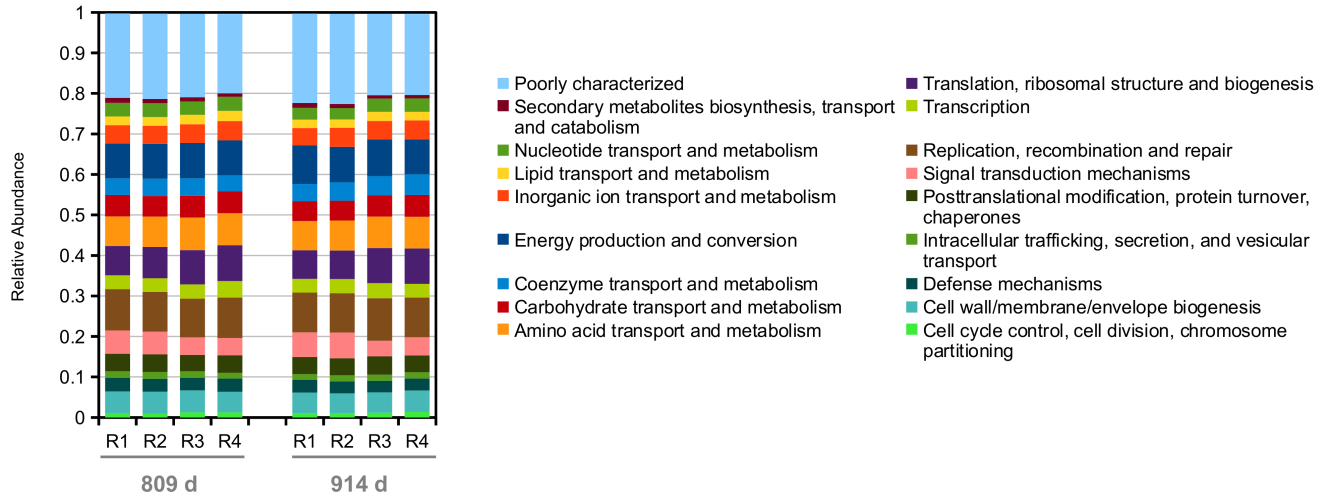
Supplementary Figure S9. Relative abundance of Level 2 categories of clusters of orthologous groups (COGs) assigned to reactor metagenomics sequencing samples.

**A. COG relative ratios and P values from ANOVA
   High vs. low ammonia**
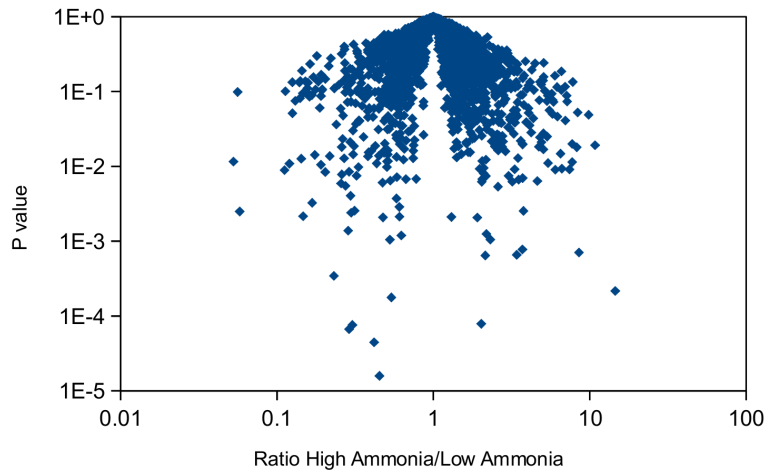
**B. COG relative ratios and P values from ANOVA
   High vs. low acetate oxidation**
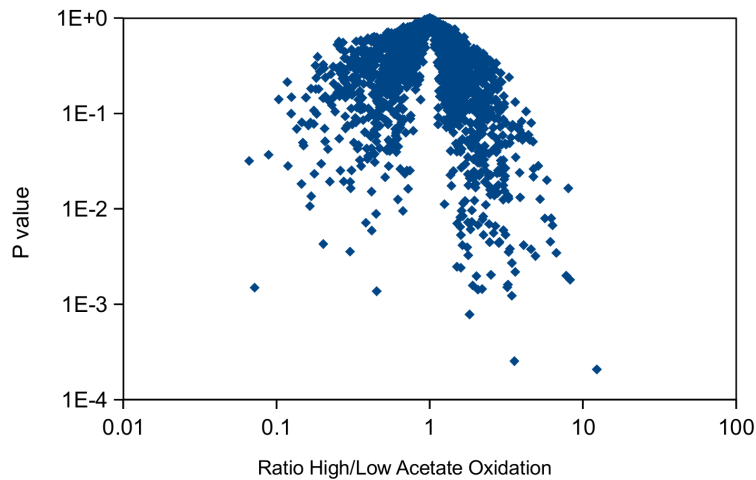
Supplementary Figure S10. Volcano plots to test significance of COG category differences between reactor conditions (from shotgun reads): (**a**) high ammonia *vs.* low ammonia and (**b**) high acetate oxidation *vs.* low acetate oxidation. A total of 2,401 COGs were identified. Ratio of relative abundances is plotted against the *p* value from ANOVA analysis comparing relative abundance values between categories.

A. COGs associated with high vs. low ammonia concentration

COG3920: CELLULAR_PROCESSES_AND_SIGNALING; Signal_transduction_mechanisms; Signal_transduction_histidine_kinase
COG3436: INFORMATION_STORAGE_AND_PROCESSING; Replication_recombination_and_repair; Transposase_and_inactivated_derivatives
COG1943: INFORMATION_STORAGE_AND_PROCESSING; Replication_recombination_and_repair; Transposase_and_inactivated_derivatives
COG3391: POORLY_CHARACTERIZED; Function_unknown; Uncharacterized_conserved_protein
COG1404: CELLULAR_PROCESSES_AND_SIGNALING; Posttranslational_modification_protein_turnover_chaperones; Subtilisin-like_serine_proteases
COG0096: CELLULAR_PROCESSES_AND_SIGNALING; Defense_mechanisms; Type_I_site-specific_restriction-modification_system_R_(restriction)_subunit_and_related_helicases
COG1572: POORLY_CHARACTERIZED; Function_unknown; Uncharacterized_conserved_protein
COG4870: CELLULAR_PROCESSES_AND_SIGNALING; Posttranslational_modification_protein_turnover_chaperones; Cysteine_protease
COG3322: CELLULAR_PROCESSES_AND_SIGNALING; Signal_transduction_mechanisms; Predicted_periplasmic_ligand-binding_sensor_domain
COG0701: POORLY_CHARACTERIZED; General_function_prediction_only; Predicted_permeases
COG1808: POORLY_CHARACTERIZED; Function_unknown; Predicted_membrane_protein
COG1215: CELLULAR_PROCESSES_AND_SIGNALING; Cell_wall_membrane_envelope_biogenesis; Glycosyltransferases_probably_involved_in_cell_wall_biogenesis
COG3269: POORLY_CHARACTERIZED; General_function_prediction_only; Predicted_RNA-binding_protein_contains_TRAM_domain
COG3875: POORLY_CHARACTERIZED; Function_unknown; Uncharacterized_conserved_protein
COG4012: POORLY_CHARACTERIZED; Function_unknown; Uncharacterized_protein_conserved_in_archaea
COG1759: POORLY_CHARACTERIZED; General_function_prediction_only; ATP-utilizing_enzymes_of_ATP-grasp_superfamily_(probably_carboligases)
COG3366: POORLY_CHARACTERIZED; Function_unknown; Uncharacterized_protein_conserved_in_archaea
COG2069: METABOLISM; Energy_production_and_conversion; CO_dehydrogenase_acetyl-CoA_synthase_delta_subunit_(corrinoid_Fe-S_protein)
COG2770: CELLULAR_PROCESSES_AND_SIGNALING; Signal_transduction_mechanisms; FOG_HAMP_domain
COG1614: METABOLISM; Energy_production_and_conversion; CO_dehydrogenase_acetyl-CoA_synthase_beta_subunit
COG2968: POORLY_CHARACTERIZED; Function_unknown; Uncharacterized_conserved_protein
COG3527: METABOLISM; Secondary_metabolites_biosynthesis_transport_and_catabolism; Alpha-acetolactate_decarboxylase
COG0786: METABOLISM; Amino_acid_transport_and_metabolism; Na_glutamate_symporter
COG3794: METABOLISM; Energy_production_and_conversion; Plastocyanin
COG5295: CELLULAR_PROCESSES_AND_SIGNALING; Extracellular_structures; Autotransporter_adhesin
COG0300: POORLY_CHARACTERIZED; General_function_prediction_only; Short-chain_dehydrogenases_of_various_substrate_specificities
COG2248: POORLY_CHARACTERIZED; General_function_prediction_only; Predicted_hydrolase_(metallo-beta-lactamase_superfamily)
COG1977: METABOLISM; Coenzyme_transport_and_metabolism; Molybdopterin_converting_factor_small_subunit
COG4604: METABOLISM; Inorganic_ion_transport_and_metabolism; ABC-type_enterochelin_transport_system_ATPase_component

COG0209: METABOLISM; Nucleotide_transport_and_metabolism; Ribonucleotide_reductase_alpha_subunit
COG0277: METABOLISM; Energy_production_and_conversion; FAD_FMN-containing_dehydrogenases
COG0552: CELLULAR_PROCESSES_AND_SIGNALING; Intracellular_trafficking_secretion_and_vesicular_transport; Signal_recognition_particle_GTPase
COG0081: INFORMATION_STORAGE_AND_PROCESSING; Translation_ribosomal_structure_and_biogenesis; Ribosomal_protein_L1
COG0327: POORLY_CHARACTERIZED; Function_unknown; Uncharacterized_conserved_protein
COG2233: METABOLISM; Nucleotide_transport_and_metabolism; Xanthine_uracil_permeases
COG2873: METABOLISM; Amino_acid_transport_and_metabolism; O-acetylhomoserine_sulfhydrylase
COG0194: METABOLISM; Nucleotide_transport_and_metabolism; Guanylate_kinase
COG0711: METABOLISM; Energy_production_and_conversion; F0F1-type_ATP_synthase_subunit_b
COG0461: METABOLISM; Nucleotide_transport_and_metabolism; Orotate_phosphoribosyltransferase
COG0233: INFORMATION_STORAGE_AND_PROCESSING; Translation_ribosomal_structure_and_biogenesis; Ribosome_recycling_factor
COG1230: METABOLISM; Inorganic_ion_transport_and_metabolism; Co_Zn_Cd_efflux_system_component
COG1327: INFORMATION_STORAGE_AND_PROCESSING; Transcription; Predicted_transcriptional_regulator_consists_of_a_Zn-ribbon_and_ATP-cone_domains
COG2030: METABOLISM; Lipid_transport_and_metabolism; Acyl_dehydratase
COG0307: METABOLISM; Coenzyme_transport_and_metabolism; Riboflavin_synthase_alpha_chain
COG1868: CELLULAR_PROCESSES_AND_SIGNALING; Cell_motility; Flagellar_motor_switch_protein
COG0230: INFORMATION_STORAGE_AND_PROCESSING; Translation_ribosomal_structure_and_biogenesis; Ribosomal_protein_L34
COG3887: CELLULAR_PROCESSES_AND_SIGNALING; Signal_transduction_mechanisms; Predicted_signaling_protein_consisting_of_a_modified_GGDEF_domain_and_a_DHH_domain
COG4294: INFORMATION_STORAGE_AND_PROCESSING; Replication_recombination_and_repair; UV_damage_repair_endonuclease
COG2117: INFORMATION_STORAGE_AND_PROCESSING; Translation_ribosomal_structure_and_biogenesis; Predicted_subunit_of_tRNA(5-methylaminomethyl-2-thiouridylate)_methyltransferase_contains_the_PP-loop_ATPase_domain
COG3364: POORLY_CHARACTERIZED; General_function_prediction_only; Zn-ribbon_containing_protein
COG2869: METABOLISM; Energy_production_and_conversion; Na-transporting_NADH:ubiquinone_oxidoreductase_subunit_NqrC
COG1118: METABOLISM; Inorganic_ion_transport_and_metabolism; ABC-type_sulfate_molybdate_transport_systems_ATPase_component
COG0321: METABOLISM; Coenzyme_transport_and_metabolism; Lipoate-protein_ligase_B
COG1730: CELLULAR_PROCESSES_AND_SIGNALING; Posttranslational_modification_protein_turnover_chaperones; Predicted_prefoldin_molecular_chaperone_implicated_in_de_novo_protein_folding
COG2132: METABOLISM; Secondary_metabolites_biosynthesis_transport_and_catabolism; Putative_multicopper_oxidases
COG4806: METABOLISM; Carbohydrate_transport_and_metabolism; L-rhamnose_isomerase
COG4641: POORLY_CHARACTERIZED; Function_unknown; Uncharacterized_protein_conserved_in_bacteria

X-axis: 0E+0, 1E-3, 2E-3, 3E-3, 4E-3, 5E-3, 6E-3, 7E-3, 8E-3 — Relative Abundance

■ Low Ammonia
■ High Ammonia

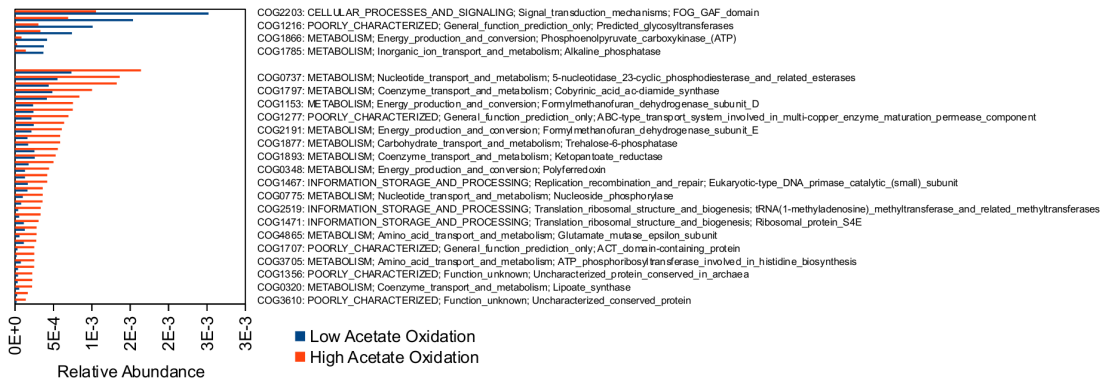## B. COGs associated with high vs. low acetate oxidation

COG2203: CELLULAR_PROCESSES_AND_SIGNALING; Signal_transduction_mechanisms; FOG_GAF_domain
COG1216: POORLY_CHARACTERIZED; General_function_prediction_only; Predicted_glycosyltransferases
COG1866: METABOLISM; Energy_production_and_conversion; Phosphoenolpyruvate_carboxykinase_(ATP)
COG1785: METABOLISM; Inorganic_ion_transport_and_metabolism; Alkaline_phosphatase

COG0737: METABOLISM; Nucleotide_transport_and_metabolism; 5-nucleotidase_23-cyclic_phosphodiesterase_and_related_esterases
COG1797: METABOLISM; Coenzyme_transport_and_metabolism; Cobyrinic_acid_ac-diamide_synthase
COG1153: METABOLISM; Energy_production_and_conversion; Formylmethanofuran_dehydrogenase_subunit_D
COG1277: POORLY_CHARACTERIZED; General_function_prediction_only; ABC-type_transport_system_involved_in_multi-copper_enzyme_maturation_permease_component
COG2191: METABOLISM; Energy_production_and_conversion; Formylmethanofuran_dehydrogenase_subunit_E
COG1877: METABOLISM; Carbohydrate_transport_and_metabolism; Trehalose-6-phosphatase
COG1893: METABOLISM; Coenzyme_transport_and_metabolism; Ketopantoate_reductase
COG0348: METABOLISM; Energy_production_and_conversion; Polyferredoxin
COG1467: INFORMATION_STORAGE_AND_PROCESSING; Replication_recombination_and_repair; Eukaryotic-type_DNA_primase_catalytic_(small)_subunit
COG0775: METABOLISM; Nucleotide_transport_and_metabolism; Nucleoside_phosphorylase
COG2519: INFORMATION_STORAGE_AND_PROCESSING; Translation_ribosomal_structure_and_biogenesis; tRNA(1-methyladenosine)_methyltransferase_and_related_methyltransferases
COG1471: INFORMATION_STORAGE_AND_PROCESSING; Translation_ribosomal_structure_and_biogenesis; Ribosomal_protein_S4E
COG4865: METABOLISM; Amino_acid_transport_and_metabolism; Glutamate_mutase_epsilon_subunit
COG1707: POORLY_CHARACTERIZED; General_function_prediction_only; ACT_domain-containing_protein
COG3705: METABOLISM; Amino_acid_transport_and_metabolism; ATP_phosphoribosyltransferase_involved_in_histidine_biosynthesis
COG1356: POORLY_CHARACTERIZED; Function_unknown; Uncharacterized_protein_conserved_in_archaea
COG0320: METABOLISM; Coenzyme_transport_and_metabolism; Lipoate_synthase
COG3610: POORLY_CHARACTERIZED; Function_unknown; Uncharacterized_conserved_protein

X-axis: 0E+0, 5E-4, 1E-3, 2E-3, 2E-3, 3E-3, 3E-3 — Relative Abundance

■ Low Acetate Oxidation
■ High Acetate Oxidation

Supplementary Figure S11. Relative abundances of identified COGs from shotgun reads with significant p values ($p<0.01$) and ratios (<0.5 or >2) for comparisons between reactor categories (from **Fig. S10**): (**a**) high ammonia *vs*. low ammonia (57 significant COGs) and (**b**) high acetate oxidation *vs*. low acetate oxidation (43 significant COGs).
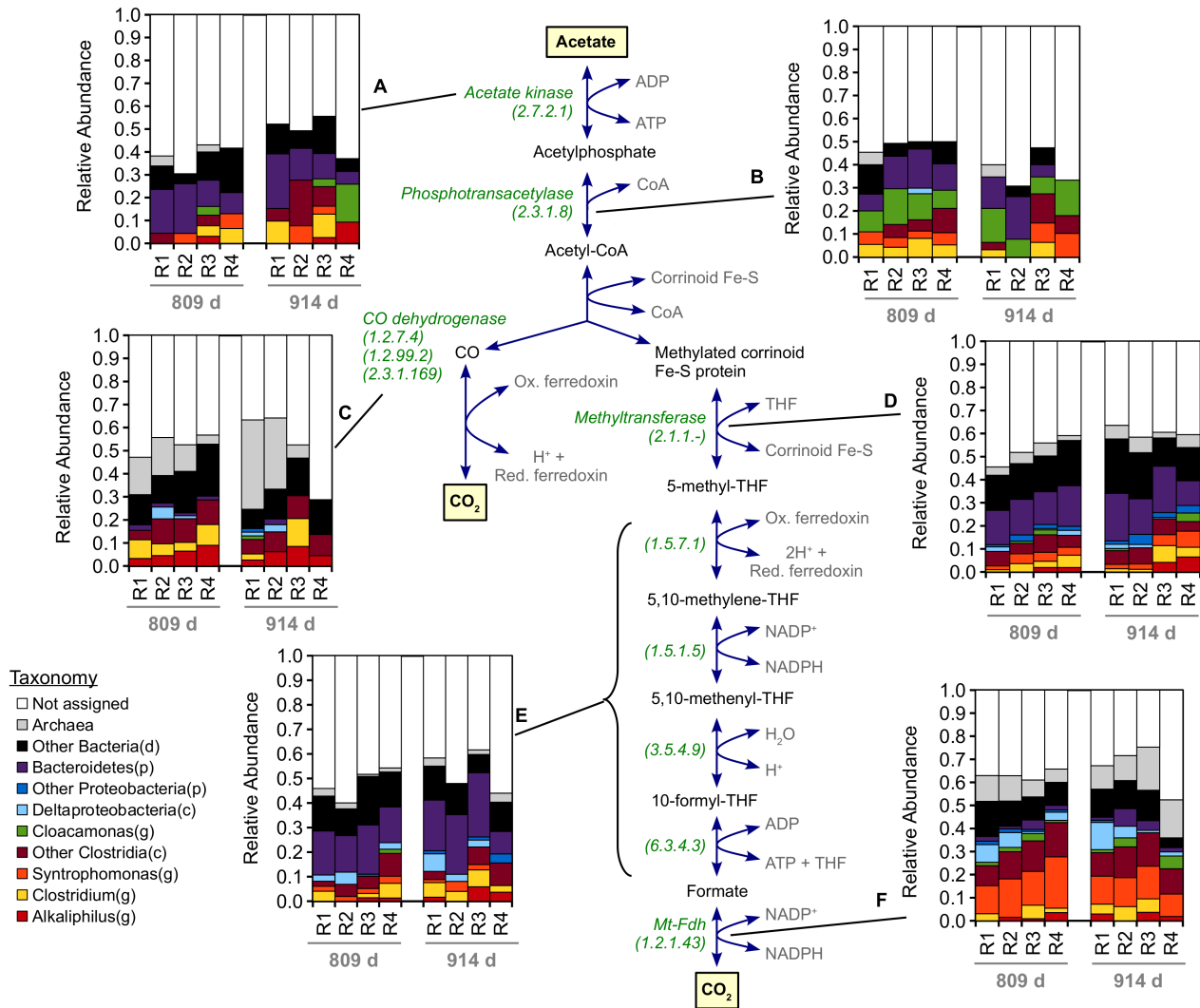
Supplementary Figure S12. Taxonomic distribution of community shotgun sequencing reads assigned to KEGG ECs potentially involved in the Wood-Ljundahl pathway (the mechanism used by anaerobic bacteria for syntrophic acetate oxidation): (**a**) **acetate kinase (EC number)** to convert acetate to acetylphosphate, (**b**) **phosphotransacetylase (EC)** to convert acetylphosphate to acetyl-CoA, (**c**) **CO dehydrogenase** to produce CO_2 and reducing equivalents from the carboxyl carbon of acetyl-CoA, (**d**) **methyltransferase (EC)** to transfer the methyl carbon to tetrahydrofolate (THF), (**e**) the series of enzymes used to produce formate and reducing equivalents from 5-methyl-THF, and (**f**) **NADP-dependent formate dehydrogenase** (EC) to form CO_2 from formate.
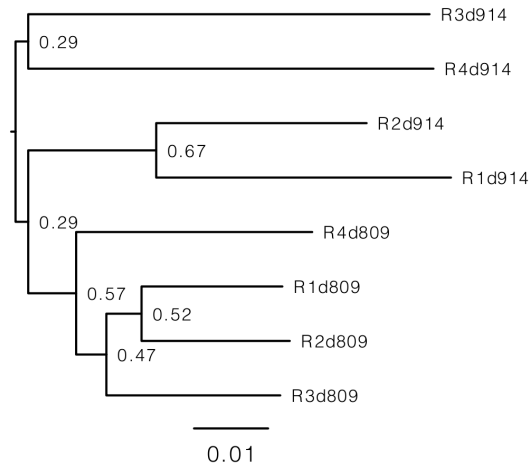
Supplementary Figure S13. Pearson distances between samples, based on KEGG EC taxonomic abundances for shotgun reads that mapped to the Wood-Ljundahl pathway (the mechanism used by anaerobic bacteria for syntrophic acetate oxidation), calculated from the abundance data shown in **Figure S12**. Bootstrap values represent support from 100 jackknifed rarefactions, 500 reads per sample. Note that samples in which syntrophic acetate oxidation was observed (R3 day 914 and R4 day 914) were outliers from the remaining samples. The distance scale is quite small, indicating that all samples were fairly well-correlated (distance = 0.01 corresponds with Pearson correlation of R=0.99, or R^2=0.98).